small methods
www.small-methods.com

Direct Measurement of the Local Electrocaloric Effect in 2D α-In_2Se_3 by Scanning Electrocaloric Thermometry

Jean Spièce, Valentin Fonck, Charalambos Evangeli, Phil S. Dobson, Jonathan M. R. Weaver, and Pascal Gehring**

The electrocaloric effect refers to the temperature change in a material when an electric field is applied or removed. Significant breakthroughs revealed its potential for solid-state cooling technologies in past decades. These devices offer a sustainable alternative to traditional vapor compression refrigeration, with advantages such as compactness, silent operation, and the absence of moving parts or refrigerants. Electrocaloric effects are typically studied using indirect methods based on polarization data, which suffer from inaccuracies related to assumptions about heat capacity. Direct methods, although more precise, require device fabrication and face challenges in studying meso- or nanoscale systems, like 2D materials, and materials with non-uniform polarization textures where high spatial resolution is required. In this study, a novel technique, Scanning Electrocaloric Thermometry, is introduced for characterizing the local electrocaloric effect in nanomaterials. This approach achieves high spatial resolution by locally applying electric fields and by simultaneously measuring the resulting temperature change. By employing AC excitation, the measurement sensitivity is further enhanced and the electrocaloric effect is disentangled from other heating mechanisms such as Joule heating and dielectric losses. The effectiveness of the method is demonstrated by examining electrocaloric and heat dissipation phenomena in 2D In_2Se_3 micrometer-sized flakes poly(vinylidene fluoride-trifluoroethylene) films.

1. Introduction

The electrocaloric effect (ECE) describes a temperature change in a material when an electric field is applied or removed. The dipoles in a dielectric material will align in the presence of an electric field, therefore reducing the configurational entropy of the system and thus, increasing its temperature (see **Figure 1**a).

Although, the effect was first predicted by William Thomson[1] in 1878, it was not observed experimentally before the mid-60s in lead zirconate (PZT). A seminal study revived the research community's interest in 2006 when a significant ECE was measured in PZT thin films,[2] opening up new strategies for solid-state cooling technologies.

From quantum technologies to air-conditioning through vaccines conservation, solid-state cooling devices represent an attractive prospect in the field of refrigeration. Their main advantage lies in their simplicity and the absence of mechanical components or refrigerants, which makes them compact, silent, extremely reliable and sustainable compared to vapor compression methods and thermoelectric materials. Furthermore, caloric heat pumping cycles have been shown to have high coefficients of performance compared to other methods.

The ECE is usually studied in polarizable materials, such as para- and ferroelectrics. In those materials, electric dipoles align with the external electric field leading to an effective polarization P. As the electric field is varied, the polarization changes and the dipole configuration entropy S increases or reduces when the dipoles are randomly oriented or align with the field, respectively. The entropy reduction, when the dipoles align with the electric field, is an exothermic process, leading to a temperature increase ΔT_{ECE} in the material. This is illustrated by the Landau–Devonshire model where the Gibbs free energy of a polarizable material can be written as follows:[3,4]

$$G = G_0 + \frac{a_0}{2}(T - T_0)P^2 + \text{ Higher order terms} \quad (1)$$

where T is the system's temperature and G_0 is a constant term containing other free energy terms independent of the polarization. T_0 and a_0 are, respectively, the Curie–Weiss temperature and the first coefficient in Landau's phase transition theory.

From this the change of entropy and temperature associated with a change of polarization can be obtained:

$$\Delta S = -\left(\frac{\partial G}{\partial T}\right)_P = -\frac{a_0}{2}P^2 \quad (2)$$

J. Spièce, V. Fonck, C. Evangeli, P. Gehring
Institute of Condensed Matter and Nanosciences
Université Catholique de Louvain (UCLouvain)
1348 Louvain-la-Neuve, Belgium
E-mail: jean.spiece@uclouvain.be; pascal.gehring@uclouvain.be
P. S. Dobson, J. M. R. Weaver
James Watt School of Engineering
University of Glasgow
Glasgow G12 8LT, UK

The ORCID identification number(s) for the author(s) of this article can be found under https://doi.org/10.1002/smtd.202401715

DOI: 10.1002/smtd.202401715

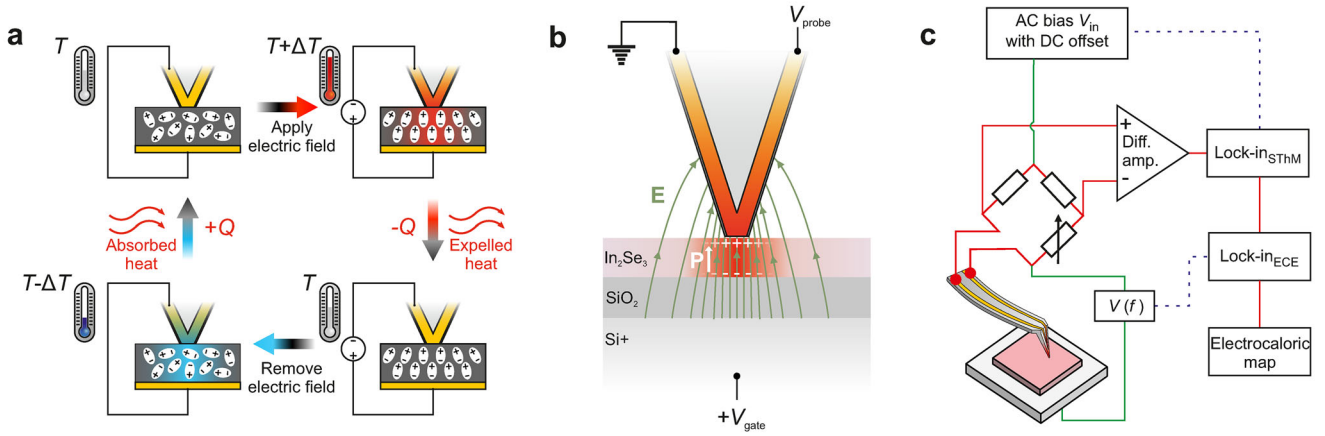

Figure 1. Electrocaloric and thermometry principles. a) Thermal cycle of the ECE effect in the material with the Scanning Thermal Microscope (SThM) probe used for applying an electric field and for the temperature measurement. b) Schematic of the electric field line distribution when approaching a sample (with a voltage V_g on the Si back gate) with a metallic probe. The polarization in the material is also shown. c) AC thermometry method employed. The signal demodulated at 91kHz in the lock-in labeled SThM is fed into the ECE lock-in for the second demodulation step which gives the final ECE map.

$$\Delta T = -T\frac{\Delta S}{C_E} = \frac{T}{2C_E}a_0 P^2 \tag{3}$$

When identifying novel materials with high electrocaloric performance and understanding the material parameters and microscopic mechanisms responsible for it, two approaches have been widely reported. On the one hand, most studies use indirect methods that rely on the measurements of the field- and temperature-dependent polarization $P(E, T)$. Using Maxwell's relations, the adiabatic temperature change can be written as $\Delta T_{ECE}^{ad} = -\int_0^{E_{max}} C_V^{-1} T \left(\frac{\partial P}{\partial T}\right)_E dE$, where C_V and E_{max} are the volumetric heat capacity and maximum applied electric field, respectively. Indirect methods suffer from the hypothesis that C_V does not depend on E leading to errors in the ΔT_{ECE}^{ad} measurement. Moreover, in most materials - especially in ferroelectrics - polarization is not linearly proportional to the electric field strength. As a result, the material's temperature change exhibits non-linear behaviour under different electric field conditions.

Direct methods, on the other hands, do not suffer from those issues, as the temperature variation is measured directly on the sample when an electric field is applyed or removed. However, accurately measuring temperature, in particular in small samples, remains challenging. The most common direct method, which avoids the need for complex microscopic thermometers, relies on infrared thermography and its lock-in variation.[5–9] Yet, due to its limited spatial resolution, this method cannot be applied to mesoscale and nanoscale systems (like 2D materials, nano-wires, nano-patterned structures, ...) or to materials with nonuniform polarization textures or nano-region domain structures.

Here, we introduce a novel method for characterizing the local electrocaloric effect in nanomaterials without the need of device fabrication. Our proposed approach exploits the high spatial resolution and the capability to directly measure local temperatures of scanning thermal microscopy (SThM). SThM has been used for electrocaloric measurements of bulk samples already[10,11] without benefiting from the high spatial resolution of the microscopy method. We achieve true locality by using the SThM probe directly to locally apply electric fields, to drive a local electrocaloric effect and to then locally measure the resulting temperature change with the same SThM probe (see Figure 1b). Furthermore, while most direct measurements schemes use DC pulses to measure the temperature rise and fall within a material, we use AC excitation[8,9] which enables high-sensitivity and the distinction between entangled effects such as the electrocaloric and Joule heating or dielectric losses. We demonstrate the excellent spatial and temperature resolution of our method by characterizing the heat dissipation and electrocaloric effects in a poly(vinylidene fluoride-trifluoroethylene) (PVDF-TrFE) thin film and 2D α-In_2Se_3 µm-sized flakes.

2. Results and Discussion

2.1. Characterization Method and Sample Preparation

Applying an electrical field to a dielectric material can trigger various effects that lead to temperature variations. The power P_C is dissipated in the dielectric with

$$P_C = fCU^2 \tan\delta \tag{4}$$

where f and U are the frequency and amplitude of the applied AC voltage, respectively, C is the capacitance of the system and δ is the loss angle of the dissipated electrical power. If there is a leakage current flowing through the dielectric with resistance R, further power due to the Joule effect is dissipated with $P_{Joule} = U^2/R$. The electric field can also align the material's dipoles and entropy is then reduced, which is countered by a temperature rise via the ECE. Then, when the field is removed, entropy increases back as dipoles start misaligning and the materials temperature decreases. In Figure 1a, a scheme of the effect under an SThM tip is shown.

We now explore electric field induced local cooling/heating effects in thick layer of In_2Se_3. We apply an AC signal with frequency f on the highly doped Si back gate electrode leading to a modulation of the electric field on the tip-sample system as:

$$\text{Bipolar:}\quad E(t) \propto V_0 \sin(\omega t) \qquad \text{Unipolar:}\quad E(t) \propto \frac{V_0}{2}(1+\sin(\omega t)) \tag{5}$$

where $\omega = 2\pi f$. As we show later, we compute the field strength using realistic finite element models.

To detect electrostatic-related temperature changes in our sample, we used a slightly modified SThM configuration (see Figure 1b). A constant force between the probe and the sample is maintained by monitoring the deflection of a laser on the back of the probe. The SThM probe consists of a Pd resistive element deposited on a triangular-shaped silicon nitride tip. The change of resistance of this element with temperature, once calibrated, allows for the reading of the probe's temperature. The typical lateral resolution for such probe is between 10 and 50 nm.[12,13] The resistive element of the probe is part of a Wheatstone bridge (see Figure 1c) and its resistance value is measured at 91 kHz via a first lock-in amplifier. This electrical resistance is converted into a SThM probe temperature using the calibration procedure as explained elsewhere.[12,13]

The back gate of the sample is modulated at the frequency f. This modulation and the SThM detection share the same electrical ground. Therefore, an electric field is applied between the tip and the sample. As described elsewhere,[14,15] we then demodulate the SThM probe temperature at the excitation frequency f and its higher harmonics, a procedure which is crucial to decouple electrocaloric and other heating effects.[9]

This lock-in detection scheme drastically increases the signal-to-noise ratio of the temperature read-out, which is very useful when studying non-steady-state effects like the ECE, as the heat that is generated during each electric polarization/de-polarization cycle vanish rapidly in the sample and can be difficult to detect using conventional DC thermometry.

2.2. Combined PFM and SThM

The proposed measurement method relies on the AC modulation of the electric field between the probe and the sample. It is therefore necessary to demonstrate that, given the SThM probe geometry, an effective field modulation exists. We thus performed finite element modeling and piezoresponse force microscopy (PFM) measurements. PFM detects oscillations in the vertical or horizontal laser deflection in response to the converse piezoelectric effect in a material under an AC field modulation.[16,17] While for PFM measurements an electrically-coated AFM tip is usually employed, here we use the SThM tip and rely on the Pd resistive thermometer to act as a ground while we apply a modulation on the back gate. In the following, we first present our PFM results and then perform finite element modeling of the tip-sample system.

To test our method, we choose PVDF-TrFE, a well-known strong ferroelectric material which has been studied extensively in our group,[18,19] and In_2Se_3, a polarizable 2D material for which several studies reported ferroelectric order due to the displacement of the middle Se atom[20–22] (see **Figure 2a**), as model systems. The 50 nm film of PVDF-TrFE was obtained by spin-coating the copolymer from a DMSO solution on a doped silicon substrate and we obtain few-layer In_2Se_3 flakes by using standard mechanical exfoliation of bulk crystals (HQ graphene) onto a doped Si wafer with 285 nm thermal oxide. We performed Raman spectroscopy on isolated flakes (see Supporting Information). Figure 2b shows a topography image of an isolated In_2Se_3 flake. For PFM experiments, we worked at the first contact resonant frequency, which in our case was around $f = 125$ kHz (see Methods), to increase the signal-to-noise ratio. The PFM amplitude and phase are shown in Figure 2d,e. Here, the vertical laser deflection signal was demodulated, but, in principle, the lateral signal can also be used. In Figure 2c, we show the SThM signal measured simultaneously with PFM, which demonstrates that the probe temperature and thus the thermal properties of the sample can be recorded at the same time as electrical fields are applied to the sample. This technique opens up new ways of investigating correlated thermal and electromechanical effects, such as polarization-dependent thermal conductivity, heat transport through domain walls or the interaction between temperature and polarization.

It is worth highlighting that PFM measurements are prone to artefacts, e.g., to short range and long range electrostatic interactions between the probe and the sample. Therefore, caution must be taken when interpreting PFM measurements obtained with this combined SThM-PFM measurement scheme. We also add that our results here are not a proof of ferroelectricity in In_2Se_3 but a demonstration of the simultaneous tip-sample field modulation and probe temperature measurements.

To estimate the electric field strength on the sample we performed finite element simulations. Results are shown in **Figure 3**. We modeled the whole SThM probe undergoing Joule heating via its Pd heater line (Figure 3a). The probe is in contact with a sample and the resulting temperature distribution of the system is shown in Figure 3b. As explained elsewhere,[12,23] we developed a model to include the tip geometry in the measurements of the probe temperature. The sensing element in this probe geometry is distributed along the triangular tip. Most of the temperature drop occurs at the end of the tip while the rest of the Pd line remains at a constant temperature.

In the same model, we implemented an electric field distribution calculation. As shown in Figure 3c, the field concentrates under the tip and mostly in the out-of-plane direction. The electric field strength at the tip-sample contact can be related to the gate voltage and flake thickness as shown in Figure 3d. We used $\varepsilon_{In2Se3} = 17$[24] for the relative permittivity of In_2Se_3. For 10 V back gate amplitude and 100 nm In_2Se_3 thickness, we obtain 500 $kVcm^{-1}$ which is beyond the coercive field required to switch polarization in In_2Se_3.[22,25]

2.3. Local ECE Measurements: Scanning Electrocaloric Thermometry (SEcT)

To drive electrocaloric effects, two AC excitation schemes were reported, the unipolar and the bipolar field modulation. In the unipolar case, electric fields with only one field direction are applied to the sample which alternate between 0 and E_{max}

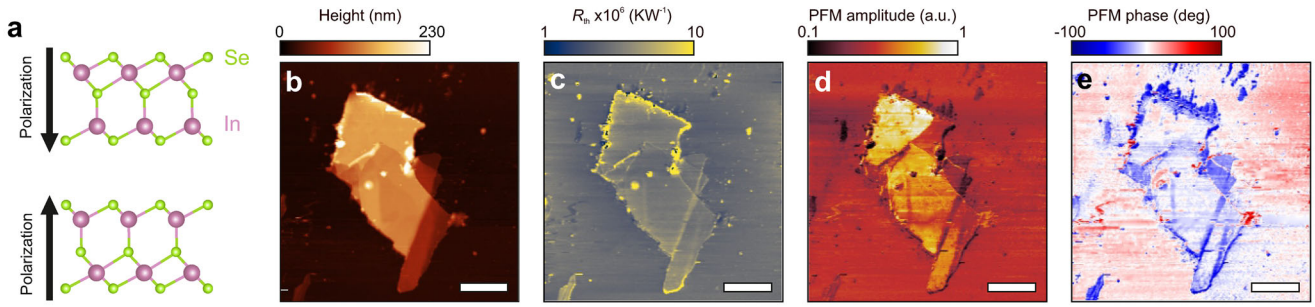

Figure 2. Combined PFM and SThM on In_2Se_3. a) Crystal structure of In_2Se_3. The main polarization axis arise from the displacement of the middle Se atom. b) Topography of the In_2Se_3 flake on the SiO_2 substrate c) SThM thermal conductance map. d,e) Piezoresponse amplitude and phase acquired simultaneously. Scale bars: 4 µm.

(leading to only positive or only negative polarization in the material), while in the bipolar case, the field alternates between $-E_{max}$ and $+E_{max}$. For bipolar field modulation at the frequency f, the polarization follows the field, but the configurational entropy linked to the dipole orientation varies with $2f$ since the relaxation happens twice per cycle. Thus, the ECE also happens at $2f$. In the case of a unipolar modulation, the oscillating electric field at f creates an entropy variation at $1f$ and the electrocaloric effect also occurs at $1f$. However, in this case, the electrocaloric temperature variation ΔT is proportional to $\delta P/\delta E = P_r \delta P_{\%}/\delta E$ with the remnant polarization P_r and $\delta P_{\%}/\delta E$ is the slope of the polarization change. If this slope is small, the temperature variation will also be small. Based on the time-dependent heat equation, we derived an analytical model of the frequency dependence for both unipolar and bipolar electrocaloric signal (see Supporting Information). In the bipolar case, no signal

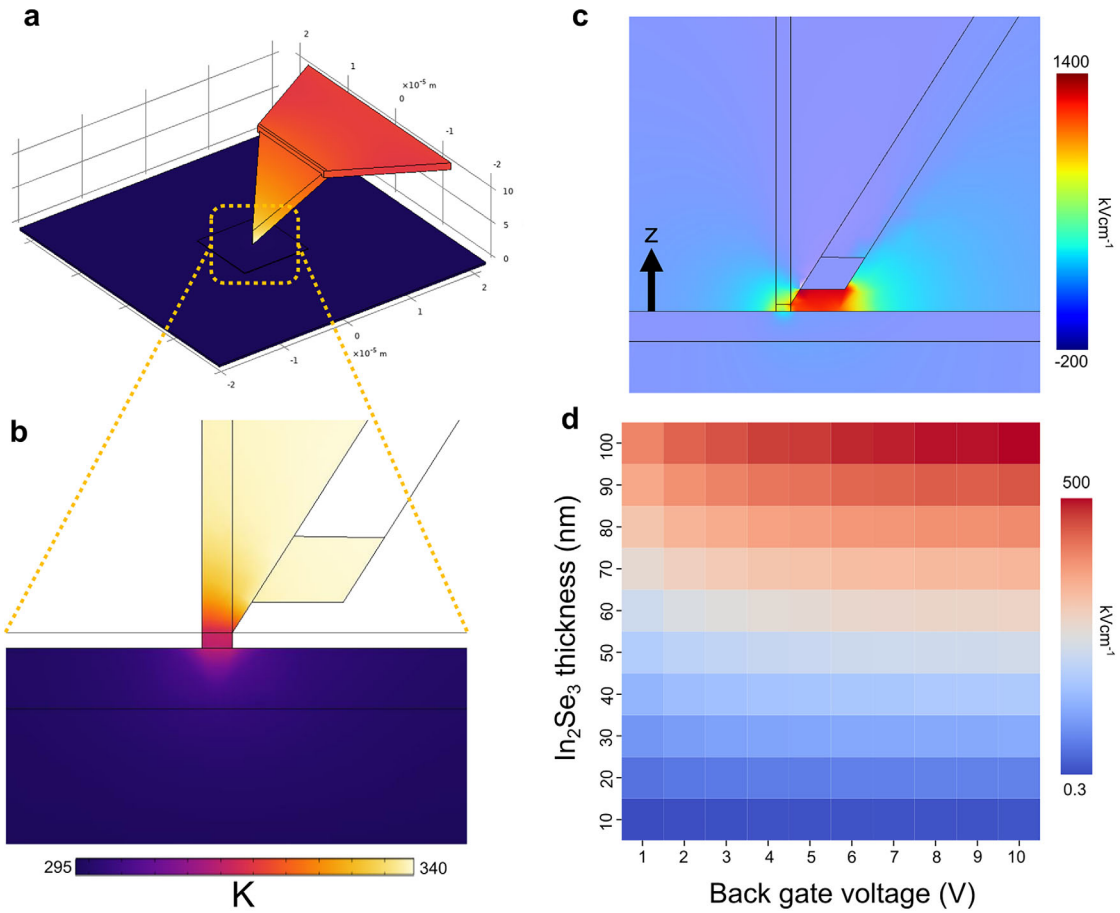

Figure 3. Finite element modeling of the tip-sample system. a) Temperature distribution in the Joule heated probe b) heat transfer between the tip and the sample. c) Electric field strength distribution in the z-direction at the tip-sample contact for a 100 nm flake and 10 V on the back gate. d) Electric field strength as a function of back gate voltage and In_2Se_3 thickness.

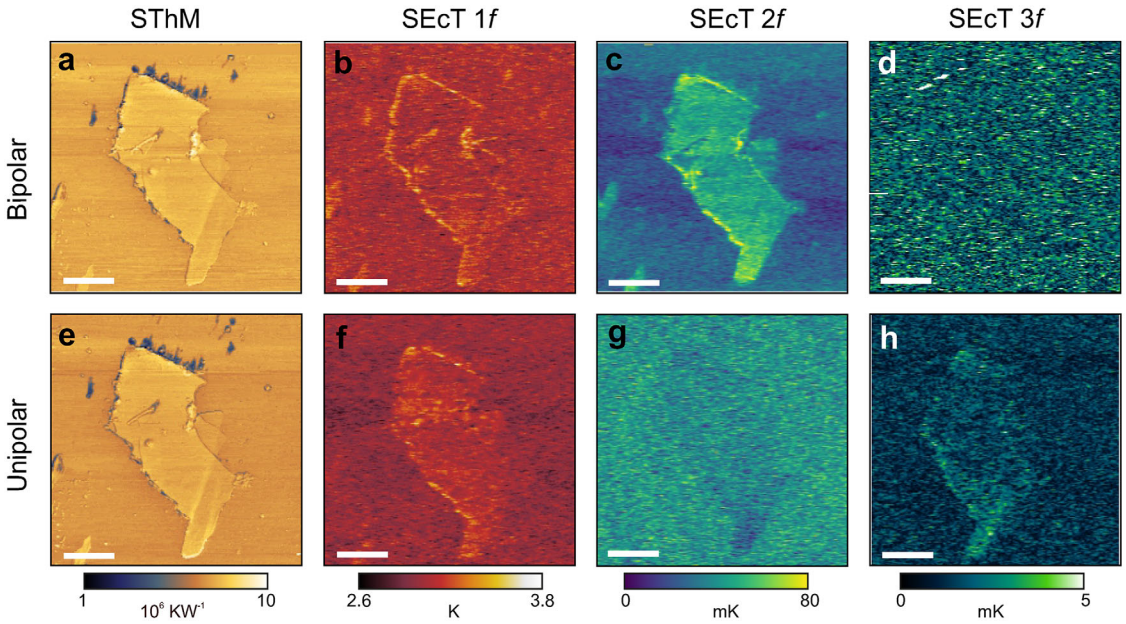

Figure 4. Electrocaloric maps of In_2Se_3. a–d) Bipolar and e–h) unipolar measurements. For both measurements, SThM, 1*f*, 2*f* and 3*f* signals are displayed. Scale bars: 4 µm.

is expected at the 1*f* and the 2*f* signal should scale quadratically with the field amplitude. For the unipolar modulation, the signal occurs in both 1*f* and 2*f* channels and also scales quadratically.

In **Figure 4**, we show the thermal resistance and the local electrocaloric maps on an In_2Se_3 flake using both unipolar and bipolar modulation. The modulation frequency of the electric field was $f = 537$ Hz and the field was modulated between 0 and $\pm E_{max} = 500$ kVcm^{-1} in the unipolar case and between $\pm E_{max} = 500$ kVcm^{-1} in the bipolar case. We simultaneously recorded the thermal resistance map and the 1*f*, 2*f* and 3*f* responses. In the Supporting Information, we also show results on a hexagonal boron nitride flake where no signal is expected, as this material is only minutely polarizable.

In Figure 4a,e, we observe a larger SThM signal on the In_2Se_3 flake than on the underlying substrate. We attribute this contrast to different tip-sample contact and thermal interface resistance between the In_2Se_3 flake and its substrate, as reported elsewhere.[23,26]

In the bipolar case, we observe a strong signal mainly in the 2*f* channel. This is expected as explained earlier by the dipole entropy variation also occurring at twice the modulation frequency. In the 1*f* response, we only observe the edges of the flake while the signal inside the flake and on the substrate have similar magnitude. We measured an average amplitude of 25 ± 6 mK on the In_2Se_3 flake.

In the unipolar case, the signal appears stronger in the 1*f* response as expected. However, as explained above, the entropy variation is small as the polarization only varies from a remnant polarization state to a full polarization state. In the 2*f* channel, we can distinguish the flake, appearing with a lower signal, from the surrounding substrate. This reduction could be explained by the lower dielectric losses between the bare silicon oxide and the In_2Se_3 flake. Finally, we observe a small response in the 3*f* signal, too. The polarization itself is not necessarily linear with field and part of the electrocaloric signal can leak into other harmonics signals. In fact, it is possible to write $P(E) = \chi_1 E + \chi_2 E^2 + \chi^3 E^3$, where χ_n is the n-th order susceptibility. Thus, part of the ECE signal can occur at the 3rd harmonic as reported by Iguchi et al.[9]

When applying an AC field to a dielectric material between two electrodes, several phenomena can generate heat. Firstly, in the presence of electrical leakage currents between the electrodes, Joule heating could contribute and manifest at the 2*f* frequency. However, for our 285 nm thick SiO_x gate dielectric, we find an electrical resistance of $\gg$10GΩ which would result in $\ll$10nW power dissipation for an amplitude of 10V. Thus, the local heating from Joule effect can be safely neglected in our samples. Secondly, dielectric losses can be present in our system and can also manifest in the 2*f* signal. The power P_C (Equation 4) dissipated in the dielectric adds a constant background of 9 ± 1 mK to the map in Figure 4d. A slight change in signal contrast is expected on the In_2Se_3 flake since the total capacitance of the system changes. Using $\varepsilon_{SiO2} = 3.9$, $\varepsilon_{In2Se3} = 17$,[24] $d_{SiO2} = 285$ nm and $d_{In2Se3} = 100$ nm we estimate a reduction of capacitance by 12% in the In_2Se_3 flake which i) cannot explain the contrast observed in Figure 4d and ii) which leads to an *under*estimation of the electrocaloric coefficient using our method as the reduced capacitance leads to reduced heat generation through the dielectric as indicated in Equation (4). Finally, in ferroelectric materials with finite electric coercivity, a change in polarization with frequency *f* would lead to hysteretic power losses $P_{hyst} \propto A_{hyst} f$, where A_{hyst} is the area of the hysteresis loop. This, however, leads to a constant (DC) heating of the sample which would not be visible in our AC experimental scheme and does not appear as a temperature drift in the SThM signal in Figure 4a.

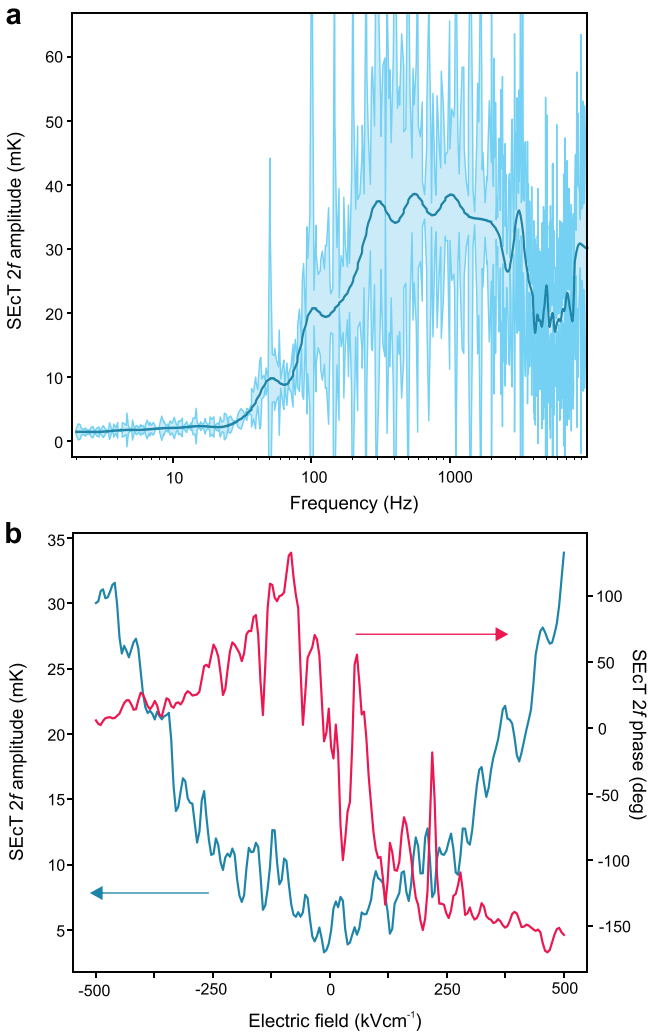

Figure 5. a) Frequency-dependence of the SEcT 2*f* amplitude signal measured at a field of ± 500 K cm kV^{-1}. We added a smoothed guideline for the eye to improve the readability. b) Electric field amplitude dependence of the 2*f* amplitude and phase signal.

2.4. Frequency and Field Dependence

We then explore the frequency and field dependence of the electrocaloric effect. To enhance the signal, we focus on bipolar modulation of the electric field. The frequency dependence is crucial for determining whether an adiabatic temperature rise is achieved. Under adiabatic conditions, the heat generated in the ECE layer exceeds the heat dissipated to the environment, allowing for a precise estimation of the ECE effect. This, in turn, facilitates comparisons with other materials.

In **Figure** 5a, we show the frequency dependence of the 2*f* electrocaloric effect. We obtained an increasing signal with increasing frequency. This is expected from a heat transport point of view. Electrocaloric heat is generated at each polarization switch cycle in the In_2Se_3 flake. If the frequency is fast enough, this heat will warm up/cool down the layer before dissipating to the environment. On the measurement side, our technique is limited by the thermalization time of the SThM sensor. For this particular type of probe, several studies reported values from few tens of µs to ms in air[27–30] which makes measurements above 10 kHz difficult, especially for higher harmonics.

Figure 5b shows the 2*f* signal amplitude and phase as a function of the electric field $\pm E_{max}$. The field dependence allows to compute the electrocaloric strength and to measure the overall behaviour of the ECE effect. As expected, the signal amplitude increases with increasing field. Indeed, a greater electric field variation allows for stronger polarization change in the material, resulting in more significant entropy change. The increase in amplitude is slightly non-linear. Non-linearities in the ECE temperature can arise from the polarization mechanisms inside the material, leading to non-linear entropy variations. This measurement enables us to compute the electrocaloric strength $\Delta T_{ECE}/\Delta E$ for In_2Se_3. We obtained 5×10^{-5} K cm kV^{-1}.

2.5. SEcT of Ferroelectric PVDF-TrFE

Finally, we apply our method to a well-studied strong ferroelectric polymer. This allows us to explore the effect of remanent polarization on the electrocaloric signal. To this end, the PVDF-TrFF copolymer film was locally polarized by applying a 20 V difference between the SThM tip and the substrate, and by scanning the sample on a 1x1 µm^2 area. Then, we performed PFM measurements by applying a 69kHz AC bias on the back electrode of the substrate. The written ferrolelectric domain is shown on the PFM amplitude image in **Figure** 6a. The PFM phase image is shown in the supplementary information. We note that the poled region appears in the PFM amplitude image because the surrounding copolymer is non-polarized, meaning it has no net polarization to induce a significant piezoelectric effect.

We then turned to SEcT to measure the temperature response of the copolymer film to an AC electric field. The results are shown on Figure 6b–d. The topography image shows the substrate on the left and the 50 nm PVDF-TrFE film on the right. The film was intentionally removed by scratching to expose the Si substrate. As expected, the polarized region is not visible in the topography image. The SThM amplitude signal shows a lower thermal resistance on the Si substrate while the copolymer films has a higher thermal resistance. It is important to note that the surface roughness plays a major role in SThM imaging and can alter the quantification of the SThM signal.[31] Nevertheless, the thermal resistance contrast observed can be explained by the difference in thermal conductivity of both materials. Importantly, the polarized region is not visible in the SThM image, indicating that the local thermal resistance remains unchanged between the polarized and non-polarized regions. A detailed combined PFM-SThM map is also shown in the Supplementary Information with the same observation.

Finally, on the SEcT map of Figure 6d, the PVDF-TrFE appears with stronger signal than the silicon substrate. Here, the image was obtained by applying a bipolar AC field modulation at 1137 Hz and with 25 V peak amplitude. The electrocaloric signal was measured at the first harmonic. A contrast is observed between the polarized region and the surrounding film: the electrocaloric signal is weaker in the polarized region. This can be attributed to the high remanent polarization in the poled region where the

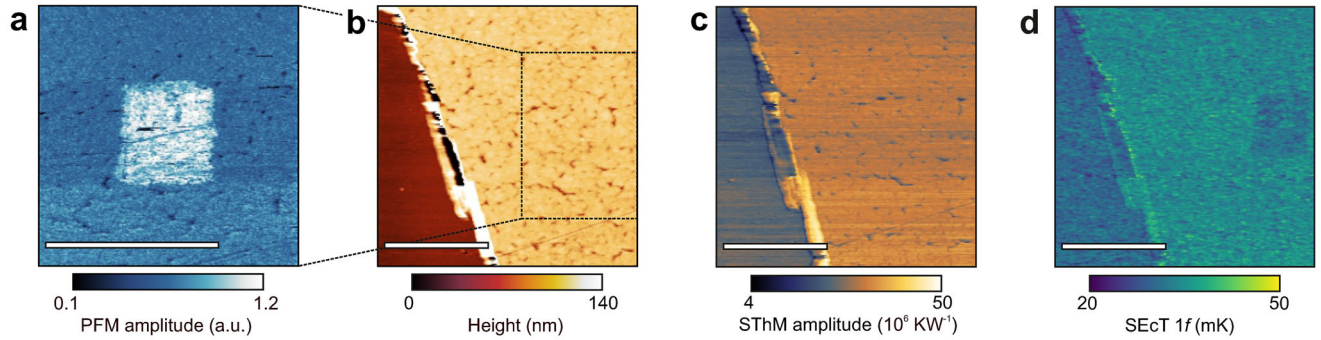

Figure 6. PFM and Electrocaloric maps of PVDF-TrFE. a) PFM amplitude map recorded at the dotted square location of (b). b–d) Topography, SThM amplitude and SEcT signal recorded on PVDF-TrFE. Scale bars: 4 µm.

field modulation is not sufficient to substantially change the polarization and create an entropy variation.

3. Conclusion

In this paper, we develop a new scanning probe microscopy method, SEcT, and show that it can be used to quantify the local electrocaloric effect in 2D materials and ferroelectric polymers. The electric field modulation applied between the probe and the sample, coupled with lock-in detection, enabled the identification of ECE signals under both bipolar and unipolar modulation schemes. The AC measurement scheme drastically improved the signal-to-noise ratio and allowed us to disentangle other components from the ECE signal. We applied the method to In_2Se_3 flakes and revealed distinct electrocaloric signal on the material with high spatial resolution, and extracted an electrocaloric strength parameter of 5×10^{-5} K cm kV^{-1}. Noteworthy, this study also introduced the combination of simultaneous PFM and SThM measurements opening new possibilities for electrothermal measurements at the nanoscale.

Because SEcT does not require the fabrication of complicated devices and can be readily applied to any meso- or nanoscale system, it represents a powerful tool for investigating electrocaloric effects in a wide range of materials, including (multiferroic) van der Waals materials and their heterostructures. Additionnaly, SEcT can be used to study the impact of nanoscale defects, domain structures, or polarization landscape on the local electrocaloric response, providing valuable insights into material properties that are otherwise difficult to access with traditional methods. Future studies may also focus on optimizing material compositions and engineering nanoscale interfaces to enhance electrocaloric performance for applications in energy-efficient cooling technologies and compact thermal devices.

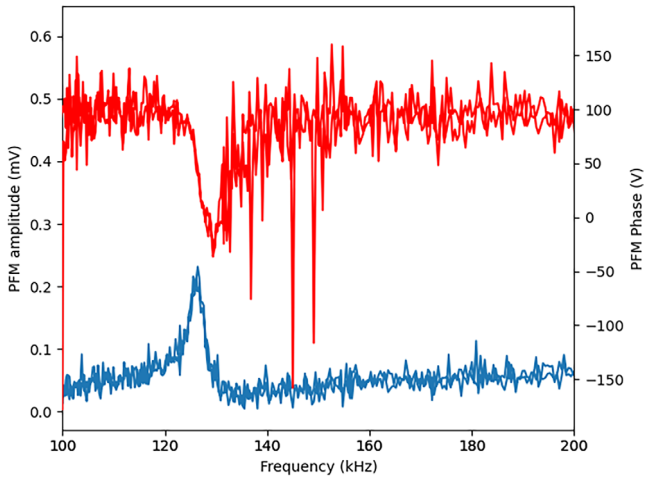

Figure 7. Frequency sweep of the amplitude and phase of the vertical PFM signal.

4. Experimental Section

Scanning Probe Microscopy and Thermometry: This work was performed on a modified Thorlabs Atomic Force Microscopy (EDU-AFM1, Thorlabs Inc.) transformed into a Scanning Thermal Microscope. The tip (Kelvin Nanotechnologies Ltd.) consists in a grooved silicon nitride cantilever with a triangular tip. On the cantilever, two gold lines are deposited and on the tip a Pd line creates the sensing element. The tip is connected to a home-made Wheatstone bridge.[32] The probe temperature is measured with a 91 kHz voltage on the bridge and demodulated with a lock-in amplifier (MFLI, Zurich Instruments Ltd.). The typical voltage drop on the tip is on the order of 0.3 V. The back gate of the sample is electrically connected with silver paste and wired to a waveform generator (DG900, Rigol inc.). The temperature of the probe is demodulated at the generator frequency and its harmonics. To record the various signals, the data acquisition capabilities of the lock-in software synchronized with the AFM scan is used.

In this study, the principles of AC-SThM thermometry as detailed elsewhere are applied.[14,15] However, the probe is different from the probe used in those studies and the sensor is spatially distributed.[12] This must be taken into account to accurately relate the sample temperature variation and the global change of the SThM probe resistance.

In Spièce et al., a model was developed including the probe geometry and relating the average probe temperature T_{av} to the system parameters:

$$T_{av} = \alpha Q_h + \beta T_m + \delta T_{air} + \gamma T_s \quad (6)$$

where α, β, γ and δ are geometry and thermal resistance factors and Q_h, T_m, T_{air} and T_s are the heater power, microscope probe base temperature, air temperature and sample temperature, respectively. If it is assumed that during the AC temperature variation of the sample, only T_s is varying, then it can be written as

$$\Delta T_s = \Delta T_{av}/\gamma \quad (7)$$

ΔT_s is the sample temperature variation. This equation includes thermal resistances and geometry in the $1/\gamma$ factor.

Contact Resonance in PFM Mode: To perform the PFM measurements reported in the main text, the back gate voltage is modulated at the first contact resonance of the probe. In **Figure 7**, the frequency sweep of the PFM amplitude and phase are plotted and the contact resonance can be observed.

Supporting Information

Supporting Information is available from the Wiley Online Library or from the author.

Acknowledgements

J.S. and V.F. contributed equally to this work. The authors acknowledge financial support from the F.R.S.-FNRS of Belgium (FNRS-CQ-1.C044.21-SMARD, FNRS-CDR-J.0068.21-SMARD, FNRS-MIS-F.4523.22-TopoBrain, FNRS-PDR-T.0128.24-ART-MULTI, FNRS-CR-1.B.463.22-MouleFrits, FNRS-FRIA-1.E092.23-TOTEM), from the EU (ERC-StG-10104144-MOUNTAIN), from the Federation Wallonie-Bruxelles through the ARC Grant No. 21/26-116, and from the FWO and FRS-FNRS under the Excellence of Science (EOS) programme (40007563-CONNECT). The authors are grateful to Prof. Bernard Nysten for providing a PVDF-TrFE sample.

Conflict of Interest

The authors declare no conflict of interest.

Data Availability Statement

The data that support the findings of this study are available from the corresponding author upon reasonable request.

Keywords

2D materials, electrocaloric effect, ferroelectricity, In_2Se_3, scanning thermal microscopy

Received: October 11, 2024
Revised: February 20, 2025
Published online:

[1] W. Thomson, *The London, Edinburgh, and Dublin Philosophical Magazine and Journal of Science* **1878**, *5*, 4.
[2] A. Mischenko, Q. Zhang, J. Scott, R. Whatmore, N. Mathur, *Science* **2006**, *311*, 1270.
[3] C. Shao, A. A. Amirov, H. Huang, *Front. Energy* **2023**, *17*, 478.
[4] A. Devonshire, *Advances in Physics* **1954**, *3*, 85, publisher: Taylor & Francis.
[5] Y. Liu, J. F. Scott, B. Dkhil, *Appl. Phys. Rev.* **2016**, *3*, 3.
[6] S. Kar-Narayan, S. Crossley, X. Moya, V. Kovacova, J. Abergel, A. Bontempi, N. Baier, E. Defay, N. Mathur, *Appl. Phys. Lett.* **2013**, *102*, 3.
[7] J. Fischer, J. Döntgen, C. Molin, S. Gebhardt, Y. Hambal, V. Shvartsman, D. Lupascu, D. Hägele, J. Rudolph, *Rev. Sci. Instrum.* **2023**, *94*, 4.
[8] S. Pandya, J. D. Wilbur, B. Bhatia, A. R. Damodaran, C. Monachon, A. Dasgupta, W. P. King, C. Dames, L. W. Martin, *Phys. Rev. Appl.* **2017**, *7*, 034025.
[9] R. Iguchi, D. Fukuda, J. Kano, T. Teranishi, K.-i. Uchida, *Appl. Phys. Lett.* **2023**, *122*, 8.
[10] O. E. Baxter, A. Kumar, J. M. Gregg, R. G. McQuaid, *J. Phys.: Energy* **2023**, *5*, 045009.
[11] L. Liao, D. Shan, C. Lei, K. Pan, J. Li, Y. Liu, *Acta Mater.* **2024**, *278*, 120264.
[12] J. Spiece, C. Evangeli, K. Lulla, A. Robson, B. Robinson, O. Kolosov, *J. Appl. Phys.* **2018**, *124*, 1.
[13] J. Spièce, C. Evangeli, A. J. Robson, A. El Sachat, L. Haenel, M. I. Alonso, M. Garriga, B. J. Robinson, M. Oehme, J. Schulze, F. Alzina, C. Sotomayor Torres, O. Kolosov, *Nanoscale* **2021**, *13*, 10829.
[14] A. Harzheim, J. Spiece, C. Evangeli, E. McCann, V. Falko, Y. Sheng, J. H. Warner, G. A. D. Briggs, J. A. Mol, P. Gehring, O. Kolosov, *Nano Lett.* **2018**, *18*, 7719.
[15] F. Menges, H. Riel, A. Stemmer, B. Gotsmann, *Rev. Sci. Instrum.* **2016**, *87*, 7.
[16] S. V. Kalinin, E. Karapetian, M. Kachanov, *Phys. Rev. B: Condens. Matter Mater. Phys.* **2004**, *70*, 184101.
[17] A. Canetta, S. Gonzalez-Munoz, V.-H. Nguyen, K. Agarwal, P. d. C. de Picquendaele, Y. Hong, S. Mohapatra, K. Watanabe, T. Taniguchi, B. Nysten, B. Hackens, R. Ribeiro-Palau, J.-C. Charlier, O. Kolosov, J. Spièce, P. Gehring, *Nanoscale* **2023**, *15*, 8134.
[18] S. Poddar, P. de Sa, R. Cai, L. Delannay, B. Nysten, L. Piraux, A. M. Jonas, *ACS nano* **2018**, *12*, 576.
[19] H. G. Kassa, R. Cai, A. Marrani, B. Nysten, Z. Hu, A. M. Jonas, *Macromolecules* **2013**, *46*, 8569.
[20] S. Xie, A. Dey, W. Yan, Z. R. Kudrynskyi, N. Balakrishnan, O. Makarovsky, Z. D. Kovalyuk, E. G. Castanon, O. Kolosov, K. Wang, A. Patanè, *2D Materials* **2021**, *8*, 045020.
[21] Q. He, Z. Tang, M. Dai, H. Shan, H. Yang, Y. Zhang, X. Luo, *Nano Lett.* **2023**, *23*, 3098.
[22] Y.-T. Huang, N.-K. Chen, Z.-Z. Li, X.-P. Wang, H.-B. Sun, S. Zhang, X.-B. Li, *InfoMat* **2022**, *4*, e12341.
[23] C. Evangeli, J. Spiece, S. Sangtarash, A. J. Molina-Mendoza, M. Mucientes, T. Mueller, C. Lambert, H. Sadeghi, O. Kolosov, *Adv. Electron. Mater.* **2019**, *5*, 1900331.
[24] D. Wu, A. J. Pak, Y. Liu, Y. Zhou, X. Wu, Y. Zhu, M. Lin, Y. Han, Y. Ren, H. Peng, Y.-H. Tsai, G. S. Hwang, K. Lai, *Nano Lett.* **2015**, *15*, 8136.
[25] S. Wan, Y. Li, W. Li, X. Mao, W. Zhu, H. Zeng, *Nanoscale* **2018**, *10*, 14885.
[26] J. Spiece, S. Sangtarash, M. Mucientes, A. J. Molina-Mendoza, K. Lulla, T. Mueller, O. Kolosov, H. Sadeghi, C. Evangeli, *Nanoscale* **2022**, *14*, 2593.
[27] E. Puyoo, S. Grauby, J.-M. Rampnoux, E. Rouvière, S. Dilhaire, *Rev. Sci. Instrum.* **2010**, *81*, 7.
[28] E. Puyoo, S. Grauby, J.-M. Rampnoux, E. Rouvière, S. Dilhaire, *J. Appl. Phys.* **2011**, *109*, 2.
[29] S. Gomès, A. Assy, P.-O. Chapuis, *Phys. Status Solidi A* **2015**, *212*, 477.
[30] P. Tovee, M. Pumarol, D. Zeze, K. Kjoller, O. Kolosov, *J. Appl. Phys.* **2012**, *112*, 11.
[31] E. Guen, P.-O. Chapuis, N. J. Kaur, P. Klapetek, S. Gomès, *Appl. Phys. Lett.* **2021**, *119*, 16.
[32] J. Spiece, *Quantitative mapping of nanothermal transport via Scanning Thermal Microscopy*, Springer Nature, New York **2019**.